ACS APPLIED MATERIALS & INTERFACES

Research Article

www.acsami.org

Development of a Stable $MnCo_2O_4$ Cocatalyst for Photocatalytic CO_2 Reduction with Visible Light

Sibo Wang, Yidong Hou, and Xinchen Wang*

State Key Laboratory of Photocatalysis on Energy and Environment, College of Chemistry, Fuzhou University, Fuzhou 350002, P. R. China

Supporting Information

ABSTRACT: The synthesis of uniform $MnCo_2O_4$ microspheres and their cooperation with a visible light harvester to achieve efficient photocatalytic CO_2 reduction under ambient conditions are reported here. The $MnCo_2O_4$ materials were prepared by a facile two-step solvothermal-calcination method and were characterized by XRD, SEM, TEM, EDX, XPS, elemental mapping, and N_2 adsorption measurements. By using the $MnCo_2O_4$ microspheres as a heterogeneous cocatalyst, the photocatalytic performance of the CO_2-to-CO conversion catalysis was remarkably enhanced, and no decrease in the promotional effect of the cocatalyst was observed after repeatedly operating the reaction for six cycles. $^{13}CO_2$ isotope tracer experiments verified that the CO product originated from the CO_2 reactant. The effect of synthetic conditions and various reaction parameters on the photocatalytic activity of the system were investigated and optimized. The stability of the $MnCo_2O_4$ cocatalyst in the CO_2 reduction system was confirmed by several techniques. Moreover, a possible mechanism for $MnCo_2O_4$-cocatalyzed CO_2 photoreduction catalysis is proposed.

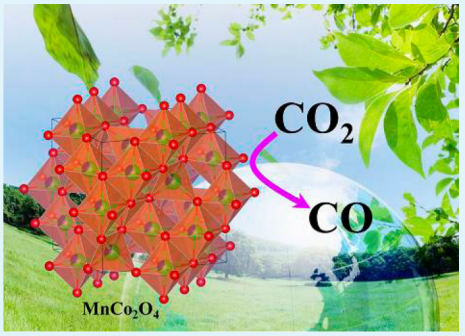

KEYWORDS: *heterogeneous photocatalysis, CO_2 reduction, $MnCo_2O_4$ microspheres, cooperative catalysis, ternary metal oxide, artificial photosynthesis*

1. INTRODUCTION

Photocatalytic CO_2 reduction by visible light has been considered the most ideal solution to diminish the increasing levels of anthropogenic CO_2, because it relies on a renewable and clean solar resource as the only energy input while providing valuable products as fuels or raw materials to partially satisfy energy demands and release some environment burden.[1−3] To achieve photocatalytic CO_2 reduction necessities the integration of light harvesters, cocatalysts, and redox assistants in a harmonious fashion to promote energy transfer and charge migration. In particular, it is well-known that the use of cocatalysts for supporting CO_2 photoreduction is a key to achieving future advancement of solar technology for CO_2 fixation, which is due mainly to the nearly inert chemical characteristic of linear CO_2 molecules.[4] As the efficiency of photochemical CO_2 reduction is intrinsically determined by the cocatalyst applied, exploiting and developing highly efficient and stable new cocatalysts to operate CO_2 conversion reactions is and will continue to be an intensively investigated subject.[5−9]

Traditionally, metal oxides, including simple binary[10−17] and complex multicomponent oxides,[18−22] are the most widely studied photocatalysts for photocatalytic CO_2 conversion. However, most of these catalysts cannot response to visible light, and their catalytic activities are still far from a level of practical utilization due to fast recombination rates of charge carriers. By virtue of cocatalysts being deposited on photocatalysts, surface heterojunctions can be established that promote charge transfer to inhibit the unwanted recombination of photogenerated electron−hole pairs and provide catalytically active sites to lower the energy barrier of the reaction.[6,23] To date, noble metals (e.g., Pt, Ru, Ir, Au, Pd, and Ag) are the repeatedly employed candidates that have served as cocatalysts in photocatalytic CO_2 reduction systems.[15,22−28] A big demerit to using these cocatalysts is their low abundance and high cost, which seriously prohibit their use in practice. Therefore, we aimed at exploring inexpensive, efficient, and stable cocatalysts for photocatalytic CO_2 fixation through artificial photosynthesis that converts CO_2 to added-value chemicals while still developing sustainable photocatalysts for solar energy conversion.[7,9,29,30]

Owing to their low cost, easy accessibility, high stability, and efficiency, cobalt-based ternary metal oxides with a spinel structure, such as $ZnCo_2O_4$, $NiCo_2O_4$, $CuCo_2O_4$, and $MnCo_2O_4$, are a family of intriguing technological materials that have attracted enormous research efforts on energy conversion areas including supercapacitors, lithium-ion batteries, and catalysis.[31−39] Among them, mixed valence $MnCo_2O_4$ has shown excellent catalytic performance for oxygen reduction reactions,[40−42] implying the potential of $MnCo_2O_4$ for catalytic reduction reactions. However, to the best of our knowledge, no reports exist describing the photocatalytic reduction of CO_2 over spinel $MnCo_2O_4$

Received: December 12, 2014
Accepted: February 3, 2015
Published: February 3, 2015

DOI: 10.1021/am508766s
ACS Appl. Mater. Interfaces 2015, 7, 4327−4335

materials as a cocatalyst. A $MnCo_2O_4$ material that combines redox active Co and Mn species in a three-dimensional nanostructure remains to be thoroughly explored in CO_2 photoreduction catalysis.

In this paper, we report facile synthesis of uniform $MnCo_2O_4$ microspheres and their cooperative functions in photocatalytic CO_2 reduction with a Ru-dye as the light harvester under benign reaction conditions. With the $MnCo_2O_4$ microspheres being used as a cocatalyst, the catalytic performance of the conversion from CO_2 to CO was remarkably promoted, and no evident decrease in this promotional effect was observed after repeating this reaction for six cycles. $^{13}CO_2$ isotope tracer experiments verified that the CO product originated from the reactant CO_2. The effect of calcination temperature and various reaction parameters on the photocatalytic activity of the reaction system were fully investigated and optimized. The stability of the $MnCo_2O_4$ cocatalyst in the CO_2 photofixation system was confirmed by several techniques, promising future development of stable $MnCo_2O_4$-based photoreduction systems for CO_2 conversion.

2. EXPERIMENTAL SECTION

2.1. Preparation of $MnCo_2O_4$ Microspheres. In the preparation of typical $MnCo_2O_4$ microspheres, 1 mmol manganese chloride tetrahydrate ($MnCl_2{\cdot}4H_2O$) and 2 mmol cobalt chloride hexahydrate ($CoCl_2{\cdot}6H_2O$) were dissolved in ethylene glycol (65 mL) and magnetically stirred for 30 min; then, 30 mmol NH_4HCO_3 powder was added.[34] After the mixture was stirred for another 30 min, the resulting homogeneous solution was transferred into a 100 mL Teflon-lined stainless-steel autoclave. The autoclave was sealed and heated at 200 °C for 20 h. After the temperature was cooled naturally, the product was collected and washed with water and absolute alcohol several times. Then, the obtained $MnCo_2O_4$ precursor was dried at 60 °C in an oven for 12 h. Lastly, the precursor was calcined at different temperatures (300, 400, 500, and 600 °C) in air atmosphere for 2 h with a ramping rate of 2 °C min^{-1} to harvest a series of $MnCo_2O_4$ products. For the convenience of discussion, unless otherwise stated, all of the $MnCo_2O_4$ samples used for the characterizations and photocatalytic reactions were prepared under calcination at 400 °C.

2.2. Characterization. Scanning electron microscope (SEM) images, energy dispersive X-ray (EDX) spectra, and the corresponding elemental mappings of the samples were collected on a Hitachi New Generation SU8010 field emission scanning electron microscope equipped with an EDX spectrometer. The samples were held on an aluminum plate. Powder X-ray diffraction (XRD) was performed on a Bruker D8 Advance instrument. Transmission electron microscopy (TEM) images, high-resolution TEM images, and selected area electron diffraction (SAED) patterns were obtained on a JEOL model JEM 2010 EX instrument. X-ray photoelectron spectra (XPS) were collected on a PHI Quantum 2000 XPS system with the C 1s peak (284.6 eV) as a reference. N_2 adsorption measurements were taken on a Micromeritics ASAP 2020 system at liquid N_2 temperature. Specific surface area was determined by the Brunauer–Emmett–Teller (BET) method. A Netzsch Thermoanalyzer (STA 449 F3) was utilized for thermogravimetric analysis (TGA) with a heating rate of 10 °C min^{-1} under an air atmosphere. A Thermo Scientific X Series II inductively coupled plasma mass spectrometry (ICP-MS) system was employed to examine the supernatant of the reaction mixture.

An Agilent 7820A gas chromatograph (thermal conductivity detector, TCD; TD-01 packed column) was utilized to analyze and quantify the products produced from the photocatalytic CO_2 conversion reactions using Ar as the carrier gas. The inlet, oven, and detector temperatures were set at 120, 50, and 200 °C, respectively. The CO produced from the $^{13}CO_2$ isotopic experiment was analyzed on an HP 5973 gas chromatography–mass spectrometer (GC–MS).

2.3. Photocatalytic CO_2 Reduction. To carry out the typical photocatalytic CO_2 reduction reaction, we added $MnCo_2O_4$ (4 μmol), $[Ru(bpy)_3]Cl_2{\cdot}6H_2O$ (10 μmol, hereafter abbreviated as Ru), solvent (5 mL, 2:3 H_2O/acetonitrile), and TEOA (1 mL) to an 80 mL reactor. Then, high purity CO_2 was introduced to the reactor with a partial pressure of 1 atm. A 300W Xe lamp with a 420 nm cutoff filter was used as the light source. During the photocatalytic reactions, the reaction system was vigorously stirred with a magnetic stirrer. The temperature of the reaction system was kept at 30 °C by cooling water unless otherwise stated. After a 1 h photocatalytic reaction, the generated products were sampled and quantified by an Agilent 7820A gas chromatograph.

3. RESULTS AND DISCUSSION

3.1. Characterization of the Samples. The $MnCo_2O_4$ precursor was first characterized by XRD. All of the diffraction peaks in the XRD patterns were indexed to those of $Mn_{0.33}Co_{0.67}CO_3$ (Figure S1, Supporting Information), which is consistent with previous work.[34] A field-emission scanning electron microscope (SEM) was used to examine the morphology. The SEM images (Figure S2, Supporting Information) reveal that uniform and well-dispersed microspheres with diameters of ~2 μm were successfully fabricated under the solvothermal conditions. Thermogravimetric analysis (TGA) was then conducted to study the thermal behavior of the $MnCo_2O_4$ precursors. Two major weight loss steps are observed in the TGA curve (Figure S3, Supporting Information). The small loss (~2.7%) below 100 °C is mainly assigned to the loss of adsorbed water, and the dominant loss is attributed to topotactic transformation of the precursor into the $MnCo_2O_4$ product and CO_2 in an air atmosphere. The second weight loss value of 35.4% is slightly higher than that of the theoretical data (32.7%), which is probably caused by the existence of strongly bound OH^- and/or blocked H_2O molecules and the shift of atoms (with the exception of CO_2 liberation) during the pyrolysis process.[34] On the basis of the TGA results, we synthesized a series of $MnCo_2O_4$ samples by calcining the precursor at 300, 400, 500, and 600 °C.

The synthesized $MnCo_2O_4$ products were subjected to characterization by powder X-ray diffraction (XRD) to investigate their crystallographic structure and phase purity. As shown in Figure 1a, all of the prepared samples exhibit sharp

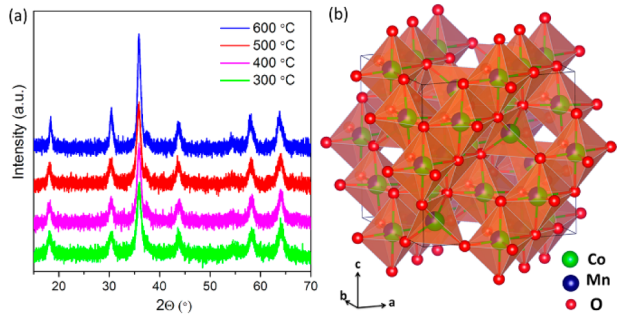

Figure 1. (a) XRD patterns of the synthesized $MnCo_2O_4$ microspheres calcined at different temperatures. (b) Structure illustration of spinel $MnCo_2O_4$.

diffraction peaks indexed as face-centered cubic $MnCo_2O_4$ (JCPDS: 23-1237). Spinel $MnCo_2O_4$ is a mixed valence ternary oxide, and in its crystal structure, the cobalt and manganese ions are dispersed over tetrahedral and octahedral stacking interstices as demonstrated in Figure 1b. No other additional diffraction peaks were detected, indicating high phase purity of the $MnCo_2O_4$ products. It is observed that elevated calcination

DOI: 10.1021/am508766s
ACS Appl. Mater. Interfaces 2015, 7, 4327–4335

temperatures produced samples with higher crystallinities, which would consequently endow them with different photocatalytic performances.

SEM and TEM measurements were conducted to examine the morphology and structure of the $MnCo_2O_4$ materials. As displayed in Figure 2a, a representative low-magnification SEM

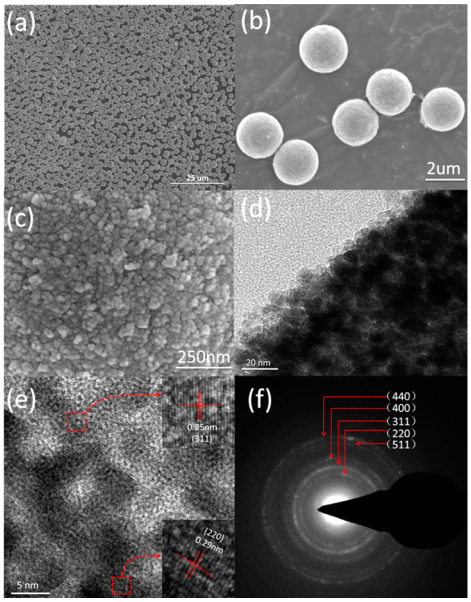

Figure 2. (a–c) Typical SEM images, (d) low-magnification and (e) high-resolution TEM images, and the (f) SAED pattern of the $MnCo_2O_4$ microspheres.

image shows that the resultant $MnCo_2O_4$ products are uniform and well-dispersed microspheres with ~2 μm diameters that are perfectly inherited from their precursors. The high-magnification SEM photographs (Figure 2b and c) demonstrate that the microspheres are actually fabricated by numerous firmly interconnected nanosized particles. The rough surface of the spheres suggests a porous structure as revealed by the TEM image (Figure 2d). Both the lattice fringes in the high-resolution TEM image (Figure 2e) and the diffraction fringes in the corresponding selected area electron diffraction (SAED) patterns (Figure 2f) are readily indexed to the interplanar spacing of a cubic $MnCo_2O_4$ structure, which indicates the formation of high crystalline samples. Uniform and high quality $MnCo_2O_4$ microspheres could also be obtained by thermally treating the precursors at other temperatures as confirmed by the SEM images in Figure S4 in the Supporting Information.

The elemental composition of the $MnCo_2O_4$ microspheres was first examined by energy dispersive X-ray (EDX) measurements. As shown in Figure 3, the EDX spectrum of the $MnCo_2O_4$ sample only gives signal peaks of Mn, Co, and O elements with a Co/Mn ratio of about 2:1. To gain insights into the elemental distribution of the $MnCo_2O_4$ spheres, we performed elemental mapping analysis, and the corresponding EDX-mapping images (Figure 3 inset) clearly elucidate homogeneous distribution of Mn, Co, and O elements in the whole spheres. The observations further confirm the formation of pure $MnCo_2O_4$ materials.

To research the valence state of the elements in the $MnCo_2O_4$ sample, we conducted XPS characterizations. As shown in Figure 4a, the survey spectrum only represents elemental peaks of Mn, Co, and O, consistent with the results

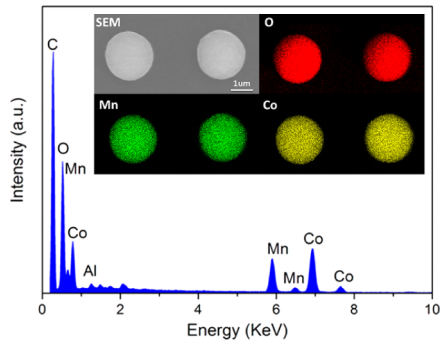

Figure 3. EDX spectrum and corresponding EDX-mapping images of a $MnCo_2O_4$ sample.

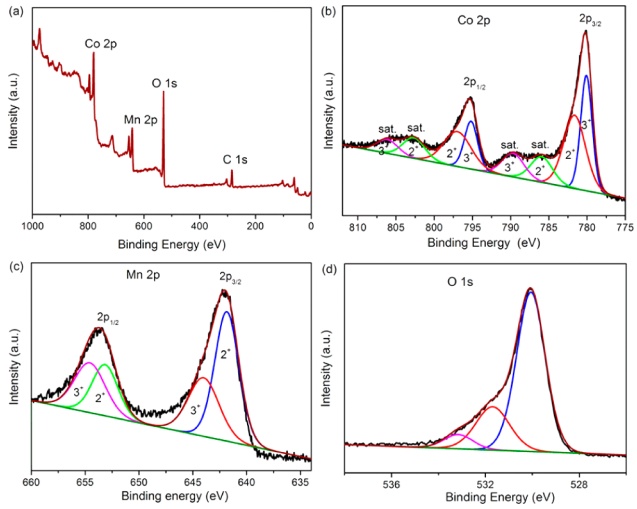

Figure 4. XPS spectra of the $MnCo_2O_4$ microspheres: (a) survey spectrum and high-resolution spectra of (b) Co 2p, (c) Mn 2p, and (d) O 1s.

of the EDX characterization. The inevitable existence of the C peak is derived from adventitious carbon species. In the high-resolution spectrum of Co 2p (Figure 4b), besides the evident satellite peaks (denoted as "sat." in the figure), two main peaks observed at 795.3 and 780.2 eV with spin–orbit splitting of ~15 eV are attributed to Co $2p_{1/2}$ and Co $2p_{3/2}$, respectively. Generally, the energy gap between the main peaks and the satellite peaks of Co 2p is very important in determining the oxidation state of cobalt. If the cation is Co^{2+}, the energy gap is ~6.0 eV, whereas the Co^{3+} cation has an energy gap of 9–10 eV.[43] After being fitted by a Gaussian fitting method, the Co 2p spectrum could be well-fitted into two spin–orbit doublets and four shakeup satellites, which are characteristic of Co^{2+} and Co^{3+} cations.[34,35] As for the Mn 2p high-resolution spectrum (Figure 4c), two main peaks at 642.0 and 653.7 eV are observed for Mn $2p_{3/2}$ and Mn $2p_{1/2}$, respectively. These two peaks could be fitted into four subpeaks, two of which are assigned to the binding energy of Mn^{3+} (644.1 and 654.6 eV) and two to Mn^{2+} (641.8 and 653.2 eV). The O 1s spectrum in Figure 4d could be divided into three photoelectron peaks at 530.2, 531.7, and 533.0 eV, which belong to lattice oxygen in the spinel structure, the oxygen of hydroxide ions, and the oxygen of physically adsorbed water molecules, respectively. The results of the XPS measurements identified the copresence of the solid-state redox couples Co^{2+}/Co^{3+} and Mn^{2+}/Mn^{3+} in the $MnCo_2O_4$

DOI: 10.1021/am508766s
ACS Appl. Mater. Interfaces 2015, 7, 4327–4335

structure,[34,35] which may endow it with numerous redox activities for heterogeneous photocatalysis and catalysis.

To investigate the specific surface area and pore characteristics of the $MnCo_2O_4$ microspheres, N_2 physical adsorption tests were carried out. As depicted in Figure 5, a type IV N_2 adsorption isotherm with a type H1 hysteresis loop was observed. This result indicates a mesoporous feature of the $MnCo_2O_4$ sample. The corresponding pore size distribution plot (Figure 5, inset) reveals that the $MnCo_2O_4$ microspheres possess a narrow pore size range of 4−11 nm and an average pore diameter of ∼7.5 nm. The generation of the mesopores is mainly ascribed to the liberation of CO_2 during the decomposition procedure by thermal treatment in air atmosphere. The specific surface area, pore volume, and pore size of the $MnCo_2O_4$ microspheres were found to be largely affected by the calcination temperature. As shown in Table 1, higher calcination temperatures resulted in $MnCo_2O_4$ materials with reduced specific surface area and pore volume but enlarged pore size. The specific surface areas of all the prepared $MnCo_2O_4$ materials are much higher than those reported by other groups.[34,35] These differences in the $MnCo_2O_4$ microspheres would ultimately influence their catalytic performance of heterogeneous CO_2 photoconversion reactions because the mesopores are in principle favorable to providing more catalytically active sites, promoting mass and charge transport, and improving CO_2 capture and adsorption.

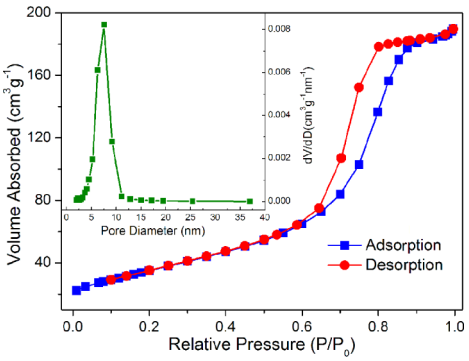

Figure 5. N_2 adsorption−desorption isotherm of the $MnCo_2O_4$ microspheres. (Inset) Corresponding pore size distribution curve calculated from the desorption branch of the N_2 isotherm by the Barrett−Joyner−Halenda (BJH) formula.

Table 1. Effects of Calcination Temperature on the BET Surface Area and Pore Parameters of the $MnCo_2O_4$ Samples

calcination temperature (°C)	S_{BET}[a] ($m^2\ g^{-1}$)	pore volume[b] ($cm^3\ g^{-1}$)	pore size[c] (nm)
300	153	0.291	6.4
400	126	0.287	7.5
500	96	0.278	9.2
600	56	0.262	14

[a]S_{BET} = BET surface area. [b]Total pore volume taken from the volume of N_2 adsorbed at ∼P/P_0 = 0.99. [c]Average pore size calculated using the desorption branch of the N_2 adsorption isotherms by the Barrett−Joyner−Halenda (BJH) method.

3.2. Photocatalytic Performance. The catalytic activity of the synthesized $MnCo_2O_4$ microspheres was evaluated by CO_2 reduction reactions with visible light irradiation under mild reaction conditions. As shown in Figure 6, when the photocatalytic reaction was operated for 1 h, a large amount of CO (27 μmol) was generated and coupled with a smaller amount of H_2 (8 μmol) without the detection of other hydrocarbons as potential products. This observation demonstrates that the chemically inert CO_2 molecules were photocatalytically converted into CO by the chemical system. However, if the $MnCo_2O_4$ cocatalyst was not added, the system only produced a very small amount of the products (1.2 μmol CO, 0.6 μmol H_2), necessitating $MnCo_2O_4$ in the photochemical reaction as a cocatalyst. Interestingly, the ratio of CO in the produced gases in the presence of the $MnCo_2O_4$ cocatalyst is much higher than that in its absence (Figure 6, inset), which may be attributed to the relatively high specific surface area (126 $m^2\ g^{-1}$) of the $MnCo_2O_4$ solid for facilitating the adsorption/concentration of CO_2 molecules. The negative control experiment shows that no products were detected when the reaction was performed in the dark, thus suggesting that the CO_2-to-CO conversion reaction is started by photocatalysis. Reference experiments determined that the CO_2 transformation reaction would not take place if the Ru photosensitizer or the sacrificial agent TEOA was excluded from the catalytic system. We also conducted a blank experiment by replacing CO_2 with Ar under otherwise identical conditions, and found that no CO was formed, which also suggests that the CO produced is derived from the CO_2 reactant.

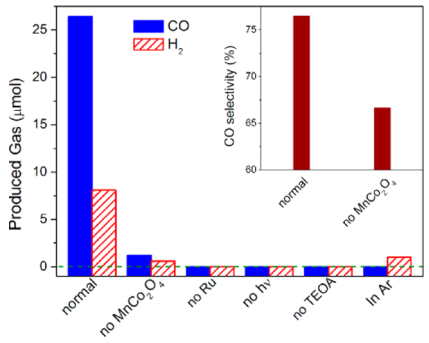

Figure 6. Production of CO and H_2 from the photocatalytic CO_2 reduction system in normal conditions relative to those of controlled experiments in conditions without the $MnCo_2O_4$ cocatalyst, Ru photosensitizer, visible light, TEOA, and using Ar place of CO_2. (inset) Corresponding selectivity of CO calculated using the equation (mol CO)/(mol (CO + H_2)).

To provide solid evidence validating the origin of the CO generated, we carried out a ^{13}C-labeled isotropic experiment by using $^{13}CO_2$ in place of $^{12}CO_2$, and the CO produced was then analyzed by GC-MS. Figure 7 shows the results of the GC-MS analysis. When $^{13}CO_2$ is the reactant, only ^{13}CO (m/z = 29) was detected, which is significantly different from the ^{12}CO (m/z = 28) detected when using $^{12}CO_2$ as the reactant. The results of this isotropic experiment validate that the CO evolution originates from photosplitting of the CO_2 molecules, not organics present in the system, and thereby strongly supports the idea that the $MnCo_2O_4$ microspheres indeed effectively accelerate photocatalytic CO_2-to-CO transformation catalysis in the current chemical system.

Studies on the reaction time demonstrate that a linear dependence between the yield of CO/H_2 and the irradiation time over the first hour of the reaction (Figure 8). The generation rates of CO and H_2 are 0.45 and 0.13 μmol min^{-1}, respectively. Thereafter, the reaction system progressively loses its high photocatalytic activity, the reason for which can mainly

DOI: 10.1021/am508766s
ACS Appl. Mater. Interfaces 2015, 7, 4327−4335

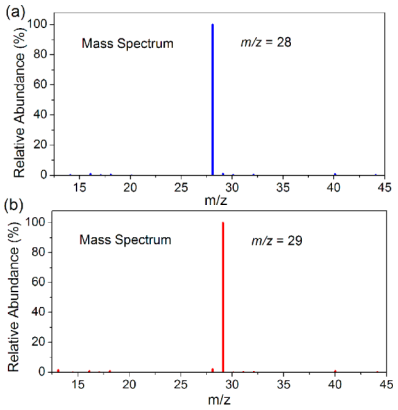

Figure 7. Results of GC-MS analysis for the CO produced from the photocatalytic CO_2 reduction reactions using (a) $^{12}CO_2$ and (b) $^{13}CO_2$.

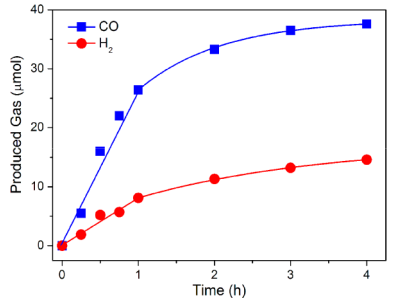

Figure 8. Yields of CO and H_2 from the CO_2 photofixation system under visible light irradiation.

be attributed to photobleaching of the Ru dye after limited catalytic operations,[44,45] but the $MnCo_2O_4$ cocatalyst is still stable to preserve its intrinsic catalytic function as will be discussed below. This observation also suggests that we should explore more robust and less costly light harvesters to cooperate with $MnCo_2O_4$ cocatalyst to establish a more stable and efficient CO_2 photofixation system for artificial photosynthesis. The accumulated generation of the product is 52 μmol after photoirradiation for 4 h, and thus affords a catalytic turnover number (TON) of 13 with respect to $MnCo_2O_4$ cocatalyst, suggesting the catalytic nature of the CO_2 conversion reaction. The obtained TON value is comparable to other reported data under similar conditions.[9,46,47]

The effect of the calcination temperature on the catalytic activity of the $MnCo_2O_4$ cocatalyst was inspected. As shown in Figure 9, obvious variations in the generation of CO/H_2 existed for the different $MnCo_2O_4$ samples. Comparing the $MnCo_2O_4$ materials calcined at 300 and 400 °C, the latter exhibited better catalytic activity because the sample annealed at 400 °C obtained higher crystallinity (Figure 1), which is beneficial for charge transfers in the photoredox reaction. However, when the calcination temperature was further elevated to 500 and 600 °C, the activities of the $MnCo_2O_4$ cocatalysts gradually reduced, which is intimately related to the sharp diminution of the specific surface area of the $MnCo_2O_4$ cocatalysts caused by the higher anneal temperatures (Table 1, entries 3 and 4). Therefore, we believe both the crystallinity and surface area of the $MnCo_2O_4$ cocatalyst are essential for determining the catalytic activity and that the optimal calcination temperature is 400 °C under the preparation conditions utilized here.

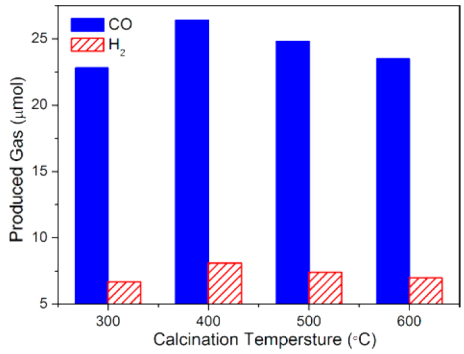

Figure 9. Generation of CO and H_2 with the $MnCo_2O_4$ cocatalyst calcined at different temperatures.

The production of CO/H_2 as a function of the wavelength of the incident light was explored. As can be seen in Figure 10, the

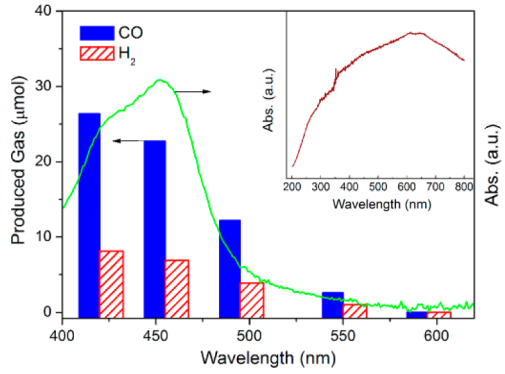

Figure 10. Wavelength-dependence of the evolution of CO/H_2 produced from the photocatalytic CO_2 reduction system. The green line is the UV–vis absorbance spectra of Ru. Insert is the solid DRS spectrum of $MnCo_2O_4$. The wavelength of the incident light was controlled by applying the appropriate long-pass cutoff filters.

yields of CO and H_2 are fundamentally dependent on the incident wavelength in a style that matches well with the adsorption intensities in the light spectrum of the Ru photosensitizer rather than those of the $MnCo_2O_4$ cocatalyst. These results reveal that the CO_2 reduction reaction proceeds photocatalytically by light excitation of the Ru dye and successive charge transport for photoredox catalysis.

To select a proper reaction medium for effectively running the photocatalytic CO_2 conversion reaction, the effects of various solvents on catalytic performance were investigated, which could be of general interest concerning CO_2 photofixation processes.[44,48,49] As shown in Figure 11, the catalytic performance of the system is significantly influenced by the reaction solvent used. When aprotic solvents, including MeCN, DMF, DMSO, and THF, were used as the reaction mediums, the catalytic system exhibited moderate catalytic activities, whereas the aprotic solvent DCM was unable to generate any products. This result is primarily attributed to the different chemical affinities between the solvent used and the CO_2 molecules because the solvents (MeCN, DMF, DMSO, THF) hold nitrogen and/or oxygen atoms that are favorable to solubilizing CO_2 through Lewis acid–base interactions.[50,51] The system also employed H_2O as a classic protic solvent, but no CO/H_2 formation was produced due mainly to the weak interaction between water and CO_2. Furthermore, the

DOI: 10.1021/am508766s
ACS Appl. Mater. Interfaces 2015, 7, 4327–4335

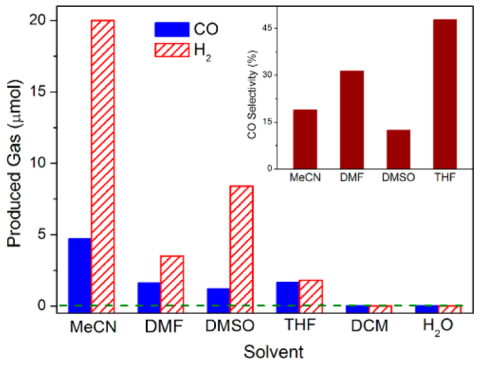

Figure 11. CO/H_2 production generated from the photocatalytic CO_2 reduction system in various solvents (DMF, *N*,*N*-dimethylformamide; DMSO, dimethyl sulfoxide; THF, tetrahydrofuran; DCM, dichloromethane).

selectivity of CO in the gases produced varied dramatically among the solvents used (Figure 11, inset).

However, remarkably enhanced catalytic activity and CO selectivity were achieved in the reaction system when using a mixture of MeCN and H_2O as the reaction medium. We thus explored the effects of the volumetric ratio of H_2O/MeCN on the catalytic performance. As listed in Table 2, upon 1 mL of

Table 2. Studies on the Effect of the Volumetric Ratio of H_2O/MeCN on the Catalytic Performance of the Reaction System[a]

entry	V_{H2O}/V_{MeCN}	CO (μmol)	H_2 (μmol)	CO:H_2 ratio
1	0/5	5	20	1:4
2	1/4	25	22	1.1:1
3	2/3	27	8	3.4:1
4	3/2	9	2	4.5:1
5	4/1	3	1	3:1

[a]Reaction conditions are the same as those of normal reactions except the volume of H_2O and MeCN in the reaction medium (5 mL) is varied.

H_2O becoming involved in the reaction medium, the catalytic activity of the CO_2-to-CO conversion reaction was drastically enhanced, presumably due to promotion of the reaction kinetics and a reduced thermodynamic barrier.[52] Additionally, adding water may also induce photolabilization of a bpy ligand from $[Ru(bpy)_3]^{2+}$ to produce the catalytically active species.[44,45] Upon the volume of H_2O being further increased to 2 mL (Table 2, entry 3), the system obtained the highest catalytic efficiency for the CO_2 splitting reaction, which is more than 5-fold improved over that of the water-free system (Table 2, entry 1). If the reaction was conducted in water-dominant mixed solutions, weakened catalytic performances were observed (Table 2, entries 4 and 5) consistent with the discussion on pure water above. Importantly, by adjusting the volumetric ratio of water/MeCN, the ratio of CO to H_2 in the products could be broadly controlled from 4.5:1 to 1:4, which renders enormous potential for the generatation of gases to be utilized as raw materials for producing liquid fuels by Fischer–Tropsch synthesis.[3]

We also carried out the photocatalytic CO_2 reduction reactions at different temperatures and found that the reaction is very susceptible to reaction temperature. As shown in Figure 12, with the reaction temperature increased from 10 to 50 °C,

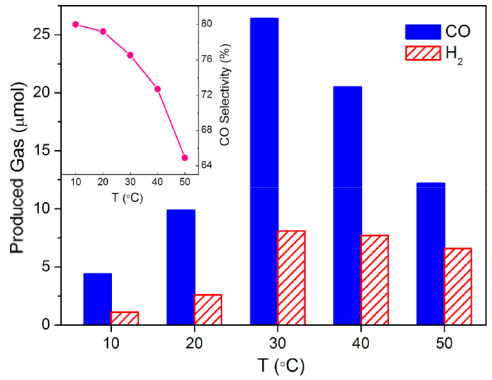

Figure 12. Evolution of CO and H_2 from the CO_2 photoreduction system at different reaction temperatures. (inset) Plot of CO selectivity versus reaction temperature.

the activity of the reaction improved at first and then observably diminished with the highest value obtained at 30 °C. The decrease in reaction activity at relatively higher temperatures is caused by unfavored absorption of CO_2 in the reaction mixture under such reaction conditions. Therefore, it was also reasonable to discover that the selectivity of CO was accordingly reduced when the reaction temperature was increased (Figure 12, inset).

To examine its stability, we filtrated the $MnCo_2O_4$ cocatalyst from the reaction mixture after the photocatalytic reactions. The obtained filtrate was analyzed by ICP-MS, and the results revealed that only <0.4% cobalt ions were detected. This filtrate was reemployed for further photocatalytic CO_2 reduction reactions under the same reaction conditions, and the cocatalytic effect was no different than in the non-cocatalytic system, indicating the heterogeneous feature of the reaction. The separated $MnCo_2O_4$ cocatalyst was then washed, dried, and reused in fresh reaction mixtures for the next photocatalytic reaction. As displayed in Figure 13, no evident decline in the

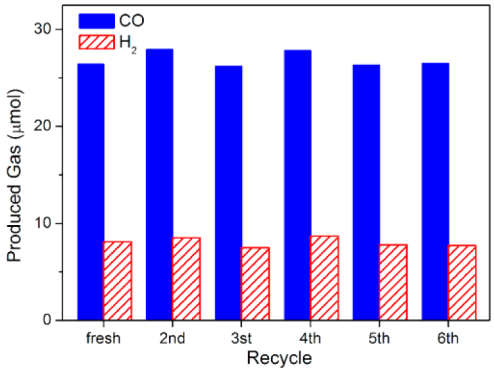

Figure 13. Formation of CO/H_2 over repeated use of the $MnCo_2O_4$ cocatalyst for stability evaluations.

production of CO/H_2 was noticed during the six repeated photocatalytic operations. In this stability test, more than 200 μmol products were generated, thus establishing a catalytic TON of ~50. Moreover, the used $MnCo_2O_4$ materials were further subjected to characterizations by SEM, XRD, and XPS. As shown in Figure 14, the morphological, crystal, and surface structures of the $MnCo_2O_4$ cocatalyst were very well kept after the photocatalytic reactions. All of the findings confirm high

DOI: 10.1021/am508766s
ACS Appl. Mater. Interfaces 2015, 7, 4327–4335

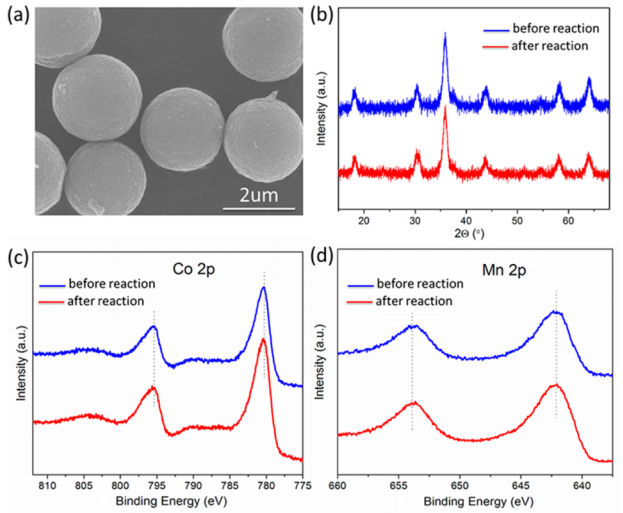

Figure 14. (a) SEM image of the $MnCo_2O_4$ microspheres after photocatalytic reactions. (b) XRD patterns, (c) Co 2p, and (d) Mn 2p high-resolution XPS spectra of the $MnCo_2O_4$ samples before and after photocatalytic reactions.

stability of the $MnCo_2O_4$ cocatalyst in the photocatalytic CO_2 conversion system.

Lastly, to explore the reaction mechanism, we evaluated the flat band potential of $MnCo_2O_4$. As shown in Figure S5 in the Supporting Information, the flat band potential of the $MnCo_2O_4$ cocatalyst is ~0.59 V (relative to NHE at pH 7.0) as determined from the Mott−Schottky analyses, endowing it with appropriate redox potential to accepted the excited electrons from the Ru complex to run the CO_2-to-CO conversion reaction (eqs 2 and 3).[52,53] A possible mechanism for the CO_2 photoreduction reaction is proposed here. With visible light irradiation, the Ru photosensitizer was excited (eq 1), generating photoinduced electrons to be transferred to the $MnCo_2O_4$ cocatalyst. Then, the CO_2 molecules absorbed on the surface of the $MnCo_2O_4$ solid were reduced to CO (eqs 2 and 3). Meanwhile, the excited electrons could also directly reduce the proton that exist in the system to generate H_2 (eq 4). The oxidized state of the Ru dye was quenched by TEOA, acting as a sacrificial electron donor (eq 5), consequently completing the photocatalytic cycle.

$$Ru(bpy)_3^{2+} + h\nu \rightarrow Ru(bpy)_3^{2+*} \quad (1)$$

$$Ru(bpy)_3^{2+*} \rightarrow Ru(bpy)_3^{3+} + e^- \quad E^{0'} = -0.87\ V \quad (2)$$

$$CO_2 + 2H^+ + 2e^- \rightarrow CO + H_2O \quad E^{0'} = -0.53\ V \quad (3)$$

$$2H^+ + 2e^- \rightarrow H_2 \quad E^{0'} = -0.41\ V \quad (4)$$

$$Ru(bpy)_3^{3+} + TEOA \rightarrow Ru(bpy)_3^{2+} + TEOA^+ \quad (5)$$

4. CONCLUSIONS

Uniform mesoporous $MnCo_2O_4$ microspheres were successfully fabricated by a simple two-step solvothermal-calcination method. The synthesized $MnCo_2O_4$ samples were systematically characterized by XRD, SEM, TEM, XPS, EDX, elemental mapping, and N_2 adsorption measurements.

The $MnCo_2O_4$ microspheres proved to be a stable cocatalyst to cooperatively operate the deoxygenative reduction of CO_2 to CO with a visible light photosensitizer under benign conditions. The origin of the CO produced was verified robustly by $^{13}CO_2$ isotope tracer experiments. The effect of calcination temperature and various reaction parameters on the catalytic performance were fully studied and optimized to manipulate effective photocatalytic CO_2 conversion reactions. The stability of the $MnCo_2O_4$ cocatalyst in the CO_2 reduction system was confirmed by several techniques. A possible reaction mechanism of the $MnCo_2O_4$-promoted CO_2 photoreduction catalysis was proposed. We are confident that the reported work will revitalize studies on CO_2 photofixations for artificial photosynthesis by employing spinel $MnCo_2O_4$ as a cost-affordable, efficient, and highly stable cocatalyst that is expected to couple with nanostructural semiconductor photocatalysts.

■ ASSOCIATED CONTENT

Supporting Information

XRD patterns, SEM images, TGA curve of the $MnCo_2O_4$ precursor, SEM images of the $MnCo_2O_4$ samples, Mott−Schottky plots of $MnCo_2O_4$, and the PL characterizations of the reaction systems. This material is available free of charge via the Internet at http://pubs.acs.org.

■ AUTHOR INFORMATION

Corresponding Author

*E-mail: xcwang@fzu.edu.cn. Phone & Fax: 86-591-83920097.

Notes

The authors declare no competing financial interest.

■ ACKNOWLEDGMENTS

This work is financially supported by the National Basic Research Program of China (2013CB632405 and 2014CB260406), National Natural Science Foundation of China (21425309), State Key Laboratory of NBC Protection for Civilian (SKLNBC2013-04K), and Specialized Research Fund for the Doctoral Program of Higher Education (20133514110003).

■ REFERENCES

(1) Listorti, A.; Durrant, J.; Barber, J. Artificial Photosynthesis: Solar to Fuel. *Nat. Mater.* **2009**, *8*, 929−930.

(2) Lewis, N. S.; Nocera, D. G. Powering the Planet: Chemical Challenges in Solar Energy Utilization. *Proc. Natl. Acad. Sci. U.S.A.* **2006**, *103*, 15729−15735.

(3) Khodakov, A. Y.; Chu, W.; Fongarland, P. Advances in the Development of Novel Cobalt Fischer−Tropsch Catalysts for Synthesis of Long-Chain Hydrocarbons and Clean Fuels. *Chem. Rev.* **2007**, *107*, 1692−1744.

(4) Sakakura, T.; Choi, J. C.; Yasuda, H. Transformation of Carbon Dioxide. *Chem. Rev.* **2007**, *107*, 2365−2387.

(5) Lehn, J. M.; Ziessel, R. Photochemical Generation of Carbon Monoxide and Hydrogen by Reduction of Carbon Dioxide and Water under Visible Light Irradiation. *Proc. Natl. Acad. Sci. U.S.A.* **1982**, *79*, 701−704.

(6) Wen, F.; Li, C. Hybrid Artificial Photosynthetic Systems Comprising Semiconductors as Light Harvesters and Biomimetic Complexes as Molecular Cocatalysts. *Acc. Chem. Res.* **2013**, *46*, 2355−2364.

(7) Wang, S.; Yao, W.; Lin, J.; Ding, Z.; Wang, X. Cobalt Imidazolate Metal−Organic Frameworks Photosplit CO_2 under Mild Reaction Conditions. *Angew. Chem., Int. Ed.* **2014**, *53*, 1034−1038.

(8) Maeda, K.; Sekizawa, K.; Ishitani, O. A Polymeric-Semiconductor−Metal-Complex Hybrid Photocatalyst for Visible-Light CO_2 Reduction. *Chem. Commun. (Cambridge, U.K.)* **2013**, *49*, 10127−10129.

DOI: 10.1021/am508766s
ACS Appl. Mater. Interfaces 2015, 7, 4327−4335

(9) Wang, S.; Ding, Z.; Wang, X. A Stable $ZnCo_2O_4$ Cocatalyst for Photocatalytic CO_2 Reduction. *Chem. Commun. (Cambridge, U.K.)* **2015**, *51*, 1517−1519.
(10) Inoue, T.; Fujishima, A.; Konishi, S.; Honda, K. Photoelectrocatalytic Reduction of Carbon Dioxide in Aqueous Suspensions of Semiconductor Powders. *Nature* **1979**, *277*, 637−638.
(11) Kohno, Y.; Tanaka, T.; Funabiki, T.; Yoshida, S. Reaction Mechanism in the Photoreduction of CO_2 with CH_4 over ZrO_2. *Phys. Chem. Chem. Phys.* **2000**, *2*, 5302−5307.
(12) Teramura, K.; Tanaka, T.; Ishikawa, H.; Kohno, Y.; Funabiki, T. Photocatalytic Reduction of CO_2 to CO in the Presence of H_2 or CH_4 as a Reductant over MgO. *J. Phys. Chem. B* **2004**, *108*, 346−354.
(13) Liao, F.; Huang, Y.; Ge, J.; Zheng, W.; Tedsree, K.; Collier, P.; Hong, X.; Tsang, S. C. Morphology-Dependent Interactions of ZnO with Cu Nanoparticles at the Materials' Interface in Selective Hydrogenation of CO_2 to CH_3OH. *Angew. Chem., Int. Ed.* **2011**, *50*, 2162−2165.
(14) Park, H.; Choi, J. H.; Choi, K. M.; Lee, D. K.; Kang, J. K. Highly Porous Gallium Oxide with a High CO_2 Affinity for the Photocatalytic Conversion of Carbon Dioxide into Methane. *J. Mater. Chem.* **2012**, *22*, 5304−5307.
(15) Sato, S.; Morikawa, T.; Saeki, S.; Kajino, T.; Motohiro, T. Visible-Light-Induced Selective CO_2 Reduction Utilizing a Ruthenium Complex Electrocatalyst Linked to a *p*-Type Nitrogen-Doped Ta_2O_5 Semiconductor. *Angew. Chem., Int. Ed.* **2010**, *49*, 5101−5105.
(16) Chen, X.; Zhou, Y.; Liu, Q.; Li, Z.; Liu, J.; Zou, Z. Ultrathin, Single-Crystal WO_3 Nanosheets by Two-Dimensional Oriented Attachment toward Enhanced Photocatalystic Reduction of CO_2 into Hydrocarbon Fuels under Visible Light. *ACS Appl. Mater. Interfaces* **2012**, *4*, 3372−3377.
(17) Mendoza, J.; Kim, H.; Park, H.; Park, K. Photocatalytic Reduction of Carbon Dioxide using Co_3O_4 Nanoparticles under Visible Light Irradiation. *Korean J. Chem. Eng.* **2012**, *29*, 1483−1486.
(18) Zhou, Y.; Tian, Z.; Zhao, Z.; Liu, Q.; Kou, J.; Chen, X.; Gao, J.; Yan, S.; Zou, Z. High-Yield Synthesis of Ultrathin and Uniform Bi_2WO_6 Square Nanoplates Benefitting from Photocatalytic Reduction of CO_2 into Renewable Hydrocarbon Fuel under Visible Light. *ACS Appl. Mater. Interfaces* **2011**, *3*, 3594−3601.
(19) Liu, Q.; Zhou, Y.; Kou, J. H.; Chen, X. Y.; Tian, Z. P.; Gao, J.; Yan, S. C.; Zou, Z. G. High-Yield Synthesis of Ultralong and Ultrathin Zn_2GeO_4 Nanoribbons toward Improved Photocatalytic Reduction of CO_2 into Renewable Hydrocarbon Fuel. *J. Am. Chem. Soc.* **2010**, *132*, 14385−14387.
(20) Liu, Q.; Wu, D.; Zhou, Y.; Su, H.; Wang, R.; Zhang, C.; Yan, S.; Xiao, M.; Zou, Z. Single-Crystalline, Ultrathin $ZnGa_2O_4$ Nanosheet Scaffolds to Promote Photocatalytic Activity in CO_2 Reduction into Methane. *ACS Appl. Mater. Interfaces* **2014**, *6*, 2356−2361.
(21) Teramura, K.; Okuoka, S. I.; Tsuneoka, H.; Shishido, T.; Tanaka, T. Photocatalytic Reduction of CO_2 using H_2 as Reductant over $ATaO_3$ Photocatalysts (A = Li, Na, K). *Appl. Catal., B* **2010**, *96*, 565−568.
(22) Iizuka, K.; Wato, T.; Miseki, Y.; Saito, K.; Kudo, A. Photocatalytic Reduction of Carbon Dioxide over Ag Cocatalyst-Loaded $ALa_4Ti_4O_{15}$ (A = Ca, Sr, and Ba) Using Water as a Reducing Reagent. *J. Am. Chem. Soc.* **2011**, *133*, 20863−20868.
(23) Zhai, Q.; Xie, S.; Fan, W.; Zhang, Q.; Wang, Y.; Deng, W.; Wang, Y. Photocatalytic Conversion of Carbon Dioxide with Water into Methane: Platinum and Copper(I) Oxide Cocatalysts with a Core−Shell Structure. *Angew. Chem., Int. Ed.* **2013**, *52*, 5776−5779.
(24) Boston, D. J.; Xu, C.; Armstrong, D. W.; MacDonnell, F. M. Photochemical Reduction of Carbon Dioxide to Methanol and Formate in a Homogeneous System with Pyridinium Catalysts. *J. Am. Chem. Soc.* **2013**, *135*, 16252−16255.
(25) Liu, J. Y.; Garg, B.; Ling, Y. C. $Cu_xAg_yIn_zZn_kS_m$ Solid Solutions Customized with RuO_2 or $Rh_{1.32}Cr_{0.66}O_3$ Cocatalyst Display Visible Light-Driven Catalytic Activity for CO_2 Reduction to CH_3OH. *Green Chem.* **2011**, *13*, 2029−2031.
(26) Sekizawa, K.; Maeda, K.; Domen, K.; Koike, K.; Ishitani, O. Artificial Z-Scheme Constructed with a Supramolecular Metal Complex and Semiconductor for the Photocatalytic Reduction of CO_2. *J. Am. Chem. Soc.* **2013**, *135*, 4596−4599.
(27) Zhang, X.; Han, F.; Shi, B.; Farsinezhad, S.; Dechaine, G. P.; Shsnkar, K. Photocatalytic Conversion of Diluted CO_2 into Light Hydrocarbons Using Periodically Modulated Multiwalled Nanotube Arrays. *Angew. Chem., Int. Ed.* **2012**, *51*, 12732−12735.
(28) Mao, J.; Ye, L.; Li, K.; Zhang, X.; Liu, J.; Peng, T.; Zan, L. Pt-Loading Reverses the Photocatalytic Activity Order of Anatase TiO_2 {0 0 1} and {0 1 0} Facets for Photoreduction of CO_2 to CH_4. *Appl. Catal., B* **2014**, *144*, 855−862.
(29) Wang, S.; Lin, J.; Wang, X. Semiconductor−Redox Catalysis Promoted by Metal−Organic Frameworks for CO_2 Reduction. *Phys. Chem. Chem. Phys.* **2014**, *16*, 14656−14660.
(30) Wang, S.; Wang, X. Photocatalytic CO_2 Reduction by CdS Promoted with a Zeolitic Imidazolate Framework. *Appl. Catal., B* **2015**, *162*, 494−500.
(31) Liu, B.; Zhang, J.; Wang, X.; Chen, G.; Chen, D.; Zhou, C.; Shen, G. Hierarchical Three-Dimensional $ZnCo_2O_4$ Nanowire Arrays/Carbon Cloth Anodes for a Novel Class of High-Performance Flexible Lithium-Ion Batteries. *Nano Lett.* **2012**, *12*, 3005−3011.
(32) Zhang, G.; Lou, X. W. General Solution Growth of Mesoporous $NiCo_2O_4$ Nanosheets on Various Conductive Substrates as High-Performance Electrodes for Supercapacitors. *Adv. Mater.* **2013**, *25*, 976−979.
(33) Kang, W.; Tang, Y.; Li, W.; Li, Z.; Yang, X.; Xua, J.; Lee, C. S. Porous $CuCo_2O_4$ Nanocubes Wrapped by Reduced Graphene Oxide as High-Performance Lithium-Ion Battery Anodes. *Nanoscale* **2014**, *6*, 6551−6556.
(34) Li, J.; Xiong, S.; Li, X.; Qian, Y. A Facile Route to Synthesize Multiporous $MnCo_2O_4$ and $CoMn_2O_4$ Spinel Quasi-Hollow Spheres with Improved Lithium Storage Properties. *Nanoscale* **2013**, *5*, 2045−2054.
(35) Fu, C.; Li, G.; Luo, D.; Huang, X.; Zheng, J.; Li, L. One-Step Calcination-Free Synthesis of Multicomponent Spinel Assembled Microspheres for High-Performance Anodes of Li-Ion Batteries: A Case Study of $MnCo_2O_4$. *ACS Appl. Mater. Interfaces* **2014**, *6*, 2439−2449.
(36) Ge, X.; Liu, Y.; Goh, F. W. T.; Hor, T. S. A.; Zong, Y.; Xiao, P.; Zhang, Z.; Lim, S. H.; Li, B.; Wang, X.; Liu, Z. Dual-Phase Spinel $MnCo_2O_4$ and Spinel $MnCo_2O_4$/Nanocarbon Hybrids for Electrocatalytic Oxygen Reduction and Evolution. *ACS Appl. Mater. Interfaces* **2014**, *6*, 12684−12691.
(37) Liu, X.; Chang, Z.; Luo, L.; Xu, T.; Lei, X.; Liu, J.; Sun, X. Hierarchical $Zn_xCo_{3-x}O_4$ Nanoarrays with High Activity for Electrocatalytic Oxygen Evolution. *Chem. Mater.* **2014**, *26*, 1891−1895.
(38) Kim, T. W.; Woo, M. A.; Regis, M.; Choi, K. S. Electrochemical Synthesis of Spinel Type $ZnCo_2O_4$ Electrodes for Use as Oxygen Evolution Reaction Catalysts. *J. Phys. Chem. Lett.* **2014**, *5*, 2370−2374.
(39) Cui, B.; Lin, H.; Liu, Y.; Li, J.; Sun, P.; Zhao, X.; Liu, C. Photophysical and Photocatalytic Properties of Core-Ring Structured $NiCo_2O_4$ Nanoplatelets. *J. Phys. Chem. C* **2009**, *113*, 14083−14087.
(40) Cheng, F.; Shen, J.; Peng, B.; Pan, Y.; Tao, Z.; Chen, J. Rapid Room-Temperature Synthesis of Nanocrystalline Spinels as Oxygen Reduction and Evolution Electrocatalysts. *Nat. Chem.* **2011**, *3*, 79−84.
(41) Liang, Y.; Wang, H.; Zhou, J.; Li, Y.; Wang, J.; Regier, T.; Dai, H. Covalent Hybrid of Spinel Manganese−Cobalt Oxide and Graphene as Advanced Oxygen Reduction Electrocatalysts. *J. Am. Chem. Soc.* **2012**, *134*, 3517−2523.
(42) Ma, T. Y.; Zheng, Y.; Dai, S.; Jaroniec, M.; Qiao, S. Z. Mesoporous $MnCo_2O_4$ with Abundant Oxygen Vacancy Defects as High-Performance Oxygen Reduction Catalysts. *J. Mater. Chem. A* **2014**, *2*, 8676−8682.
(43) Wei, W.; Chen, W.; Ivey, D. G. Rock Salt−Spinel Structural Transformation in Anodically Electrodeposited Mn−Co−O Nanocrystals. *Chem. Mater.* **2008**, *20*, 1941−1947.
(44) Ziessel, R.; Hawecker, J.; Lehn, J. M. Photogeneration of Carbon Monoxide and of Hydrogen via Simultaneous Photochemical Reduction of Carbon Dioxide and Water by Visible-Light Irradiation of Organic Solutions Containing Tris(2,2′-bipyridine)ruthenium(II)

DOI: 10.1021/am508766s
ACS Appl. Mater. Interfaces 2015, 7, 4327−4335

and Cobalt(II) Species as Homogeneous Catalysts. *Helv. Chim. Acta* **1986**, *69*, 1065−1084.
(45) Lehn, J. M.; Ziessel, R. Photochemical Reduction of Carbon Dioxide to Formate Catalyzed by 2,2′-Bipyridine- or 1,10-Phenanthroline-Ruthenium(II) Complexes. *J. Organomet. Chem.* **1990**, *382*, 157−173.
(46) Chai, Z.; Li, Q.; Xu, D. Photocatalytic Reduction of CO_2 to CO Utilizing a Stable and Efficient Hetero−Homogeneous Hybrid System. *RSC Adv.* **2014**, *4*, 44991−44995.
(47) Andrade, G. A.; Pistner, A. J.; Yap, G. P. A.; Lutterman, D. A.; Rosenthal, J. Photocatalytic Conversion of CO_2 to CO Using Rhenium Bipyridine Platforms Containing Ancillary Phenyl or BODIPY Moieties. *ACS Catal.* **2013**, *3*, 1685−1692.
(48) Liu, B. J.; Torimoto, T.; Matsumoto, H.; Yoneyama, H. Effect of Solvents on Photocatalytic Reduction of Carbon Dioxide using TiO_2 Nanocrystal Photocatalyst Embedded in SiO_2 Matrices. *J. Photochem. Photobiol., A* **1997**, *108*, 187−192.
(49) Matsuoka, S.; Kohzuki, T.; Pac, C.; Ishida, A.; Takamuku, S.; Kusaba, M.; Nakashima, N.; Yanagida, S. Photocatalysis of Oligo (*p*-Phenylenes): Photochemical Reduction of Carbon Dioxide with Triethylamine. *J. Phys. Chem.* **1992**, *96*, 4437−4442.
(50) Kazarian, S. G.; Vincent, M. F.; Bright, F. V.; Liotta, C. L.; Eckert, C. A. Specific Intermolecular Interaction of Carbon Dioxide with Polymers. *J. Am. Chem. Soc.* **1996**, *118*, 1729−1736.
(51) Kim, K. H.; Kim, Y. Theoretical Studies for Lewis Acid−Base Interactions and C−H···O Weak Hydrogen Bonding in Various CO_2 Complexes. *J. Phys. Chem. A* **2008**, *112*, 1596−1603.
(52) Schneider, J.; Jia, H.; Muckerman, J. T.; Fujita, E. Thermodynamics and Kinetics of CO_2, CO, and H^+ Binding to the Metal Centre of CO_2 Reduction Catalysts. *Chem. Soc. Rev.* **2012**, *41*, 2036.
(53) Kalyanasundaram, K. Photophysics, Photochemistry and Solar Energy Conversion with Tris(bipyridyl)ruthenium(II) and Its Analogues. *Coord. Chem. Rev.* **1982**, *46*, 159.

DOI: 10.1021/am508766s
ACS Appl. Mater. Interfaces 2015, 7, 4327−4335